Electron Transport Layer Optimization for All-Inorganic, Vacuum-Deposited Perovskite-Based Photodiodes with Improved Reverse Bias Stability and High Speed

Athina Papadopoulou[1,2*], Maria Isabel Pintor-Monroy[1*], Sreeshma Dayaran[3], Irina Skvortsova[4], João Pedro de Sousa Gouveia dos Anjos[1,6], Sownder Subramaniam[1,2], Wenya Song[1], Itai Lieberman[1], Yinghuan Kuang[1], Johan Hofkens[3,7], Maarten B. J. Roeffaers[5], Sara Bals[4], Robert Gehlhaar[1], and Jan Genoe[1,2]

[1]imec, Kapeldreef 75, 3001 Leuven, Belgium
[2]Department of Electrical Engineering (ESAT), KU Leuven, Kasteelpark Arenberg 10, 3001 Leuven, Belgium
[3]Department of Chemistry, Faculty of Sciences, KU Leuven, 3001 Leuven, Belgium
[4]Electron Microscopy for Materials Research, University of Antwerp, 2020 Antwerp, Belgium
[5]cMAS, Department of Microbial and Molecular Systems, KU Leuven, Celestijnenlaan 200F, 3001 Leuven, Belgium
[6]i3N/CENIMAT, Department of Materials Science, Faculty of Science and Technology, Universidade NOVA de Lisboa and CEMOP/UNINOVA, Campus de Caparica, 2829-516 Caparica, Portugal
[7]Max Planck Institute for Polymer Research, 55128 Mainz, Germany

Keywords: Perovskite, Inorganic, Thermal Evaporation, Photodetector, Reverse Bias, Stability, Variability, Response Speed

1. Abstract

Having proven their potential as visible and near infrared light detectors, metal halide perovskites are now being integrated with thin-film transistor- or silicon-based read-out circuits for high-resolution imaging applications. Vacuum-deposited, all-inorganic perovskite photodiodes (PePDs) offer a superior alternative to solution-processed hybrid organic-inorganic perovskites, addressing their specific limitations in semiconductor fabrication process compatibility. Specifically, vacuum processing overcomes challenges related to limited scalability and reproducibility, while the development of photodiodes made entirely of inorganic compounds improves their resilience at high-temperature environments. At the same time, the performance of vacuum-deposited, all-inorganic PePDs has proved competitive with that of their solution-processed hybrid organic-inorganic counterparts. Building on this progress, this study demonstrates that the careful tuning of the electron transport layer (ETL) can achieve a three-fold optimization in the performance of all-inorganic, vacuum deposited PePDs, through improvements in device performance repeatability, operational stability under reverse bias, and carrier extraction speed. Specifically, we identify that the combination of a fullerene and a metal oxide transport layer, as well as the careful tuning of their respective thicknesses, can simultaneously prevent metallic shorts, reduce the amount of interface defect states, and extend the depletion width of the photodiode. Eventually, the optimized photodiodes exhibit minimal variability in device performance, maintaining a stable dark current density below 0.1 μA/cm^2 even after biasing at -2 V for 1 hour. They also demonstrate a rise time below 2 μs, with results confirming the potential for sub-μs response times for further scaled down pixel sizes.

2. Introduction

Almost 15 years of intensive scientific research has established metal halide perovskites as a leading candidate for highly efficient commercial solar cells, particularly when used in tandem architectures[1,2]. The efforts to optimize the perovskite quality and device performance have sparked interest in numerous other optoelectronic applications, including photodetectors[3–7], light-emitting diodes[8,9], and lasers[10,11]. In the case of photodetector applications, the use of perovskites has been demonstrated across a wide range

of photon energies, spanning from the near-infrared[12] all the way to X-rays[13–17]. Even in the visible spectrum, where silicon is the standard detector material, perovskites offer competitive advantages, mainly related to their high absorption coefficient[18] and fast response time[19]. In this framework, perovskite photodetectors were recently successfully integrated atop a silicon read-out circuit, paving the way for fast and high-resolution perovskite imagers[20–22].

To enhance the compatibility of PePDs with CMOS fabrication processes, it is essential to re-evaluate the deposition technique and thermal stability of the films. Among deposition methods, solution processing—particularly spin coating—is the most widely used one due to its accessibility and versatility[23]. However, it falls short in scalability and reproducibility[24], in contrast to physical vapor deposition methods, such as thermal evaporation, which align better with the standards of silicon-integrated structures[25]. Additionally, hybrid organic-inorganic perovskite thin films have proved highly effective for the development of efficient solar cells. Yet, the presence of volatile organic compounds compromises the thermal stability of these films. For instance, it has been demonstrated that at temperatures exceeding 100°C, methylammonium lead iodide perovskites ($MAPbI_3$) decompose into methylamine, hydrogen iodide, and lead iodide, resulting in the loss of their photoconverting properties.[26]. This limitation makes solution-processed perovskites unsuitable for many semiconductor integration processes, underscoring the advantages of inorganic perovskites, which can withstand temperatures exceeding 250°C[27]. Among inorganic perovskites, $CsPbI_2Br$ is particularly favoured for its optimal bandgap (~1.92 eV) suitable for visible light detection and its enhanced stability in the black phase[28]. Consequently, the development of efficient, vacuum-deposited, all-inorganic PePDs could be pivotal for the seamless integration of perovskites into silicon fabrication processes.

While the use of inorganic, vacuum deposited perovskite layers for the fabrication of solar cells or photodetectors has gained significant attention over the past years[15,29–32], most of these studies still employ organic and/or solution processed additives, as well as passivation and charge transport layer. This practice usually boosts the device's performance, however, it counteracts the benefits of using inorganic and vacuum processed perovskites. The number of reports that develop perovskite-based heterojunctions where all layers are inorganic, and vacuum processed is still minimal[33–35]. In this work, we follow up on our previous report that demonstrated the use of co-evaporated $CsPbI_3$ perovskites for the fabrication of all-inorganic, vacuum-deposited photodetectors[35]. Despite its improved thermal stability and competitive performance, the black (or photoactive) $CsPbI_3$ phase is only stable at temperatures beyond 320 °C[36]. It is possible to kinetically trap the black phase at room temperature in inert environments through rapid cooling, however the photoinactive (yellow) phase emerges almost instantaneously upon exposure to moderate temperatures (~60 °C) or ambient moisture[37]. To address this, we introduce Br-doping in the $CsPbI_3$ absorber, shifting to the $CsPbI_2Br$ composition, effectively enhancing the phase stability of the absorber in the ambient environment through an increase of the perovskite's tolerance factor and lattice strain (**Figure S1**)[38,39]. Additionally, we demonstrate that by simply tuning the architecture of the electron transport layer, we can achieve a three-fold optimization in performance variability, reverse bias stability, and carrier extraction speed. Specifically, we identify that using thermally evaporated C_{60} as the sole electron transport layer (ETL) results in significant variability in device performance. Additionally, e-beam deposited TiO_2 introduces interface defect states that lead to reverse bias breakdown. While this mechanism has been studied extensively in perovskite-based solar cells (PeSC)[40–45], it is often overlooked in PePDs, where studies typically focus on dynamic current-voltage scans or limit the operating range to small reverse biases up to -0.5 V[16,46–48]. We demonstrate that implementing an ETL with sequentially deposited C_{60} and TiO_2 layers can effectively address both challenges, ensuring consistent device performance and limiting the dark current to values below 1 $\mu A/cm^2$, even after 60 minutes of biasing at -2 V. Furthermore, we show that the thickness of C_{60} in this bilayer configuration is crucial not only for maintaining a defect-free interface but also for enhancing the extraction speed of photo-generated carriers by extending the diode's depletion width.

3. Results and Discussion

For the fabrication of all-inorganic, all-evaporated perovskite photodiodes we used a p-i-n device architecture, with commercial indium tin oxide (ITO) as the common contact and a DC sputtered nickel oxide layer (NiO_x) as the hole transport layer (HTL). The cesium lead iodide bromide perovskite, with a nominal stoichiometry of $CsPbI_2Br$, was deposited via the thermal co-evaporation of CsBr and PbI_2 powders. After the perovskite deposition, the stack was flash annealed at 300 °C in nitrogen environment to achieve films with larger grains and improved crystallinity. A comprehensive analysis of the perovskite film's structural, morphological, and optical properties is provided in our previous work[49]. For the deposition of the ETL, two candidates were evaluated: e-beam evaporated titanium oxide (TiO_2) and thermally evaporated buckminsterfullerene (C_{60}). The stack was completed with the evaporation of aluminum (Al) top contacts, defined via the use of a shadow mask. The cross-section schematic of the stack configuration is shown in **Fig. 1a**, while **Fig. 1e** depicts the energy levels of each layer. The band structures for Al, ITO, NiO_x, C_{60}, and TiO_2 were previously characterized within our group[50,51] and the band structure of the $CsPbI_2Br$ layer is referenced from literature[52].

Similarly to our previous work on all-evaporated, all-inorganic perovskite photodiodes[35], we start by evaluating the use of e-beam deposited TiO_2 as the stack's ETL (Sample 40TiO_2 in **Fig. 1b**). TiO_2 is a widespread ETL in perovskite-based optoelectronic devices, owing to its excellent hole-blocking capability, appropriate energy alignment with perovskite absorbers, and high optical transparency[53]. TiO_2 is most commonly deposited via spin-coating to form either a mesoporous or compact layer[54]. However, sufficient studies have also explored its deposition using vacuum-based techniques, including electron-beam evaporation[55], magnetron sputtering[56], and atomic layer deposition (ALD)[57]. In the case of sample 40TiO_2, the conformal deposition of all layers, as well as the absence of pinholes or cracks in the perovskite layer, is confirmed through scanning transmission electron microscopy (STEM) on a focused ion beam (FIB)-prepared cross-section (**Fig. 1f**). The excellent homogeneity of the fabrication process is further demonstrated by the nearly identical current density – voltage (J-V) characteristics (**Fig. 2a**) across 12 devices fabricated on the same sample (**Fig. S3a**). Specifically, the solid line represents the median response of the 12 devices under both dark and 1-sun illumination conditions, while the shaded area indicates the interquartile range (IQR). At –2 V, the median current density is 2.4 μA/cm² in the dark 11.33 mA/cm² under 1-sun illumination. The corresponding IQR values are 0.51 μA/cm² and 1.45 mA/cm², respectively. The discrete J-V curves for each device can be found in **Fig. S3b**. Finally, the EQE spectral response of a single device (**Fig. S4a**) reveals that the EQE becomes fully saturated -1 V and is higher than 70% across the complete visible spectrum.

The accurate determination of a device's dark current (J_d) is critical for its proper characterization, as well as for the evaluation of other important parameters, such as its specific detectivity. Dynamic voltage scans of perovskite-based photodiodes are highly sensitive to the speed and direction of measurement because they are influenced by charging and capacitive effects as well as ion migration. As a result, the monitoring of the steady-state current under steps of constant bias is considered more reliable[46,47,58]. The elimination of transient currents during steady-state scans is manifested as a sharp drop of J_d within the first tens of seconds under reverse bias, often resulting nearly an order-of-magnitude reduction in dark current for a specific biasing point compared to values observed in dynamic J-V scans. In the scope of this study, we perform static measurements, where J_d is measured as a function of time for 300 seconds at consecutive reverse bias steps. Between two consecutive steps, the device was allowed to reset in the dark for an additional 300 seconds. The results for sample 40TiO_2, which are illustrated in **Fig. 2d**, indicate that J_d saturates below 0.1 μA/cm^2 at the end of the static scan at -0.5 and -1 V, however a 3-order-of-magnitude increase is observed once the bias is increased to -2 V. This effect, which is concealed during the dynamic J-V scan, could be detrimental to photodetector applications that require reverse biasing for an extensive period of time. The nature of this phenomenon is reversible, as demonstrated through J-V scans for the same device before and after the static measurements (**Fig. S5**).

This multiple-order-of-magnitude increase in J_d is known as a reverse bias breakdown of perovskite-based diodes. This mechanism has been previously investigated in the context of PeSCs that fall under reverse bias conditions when a shadowed cell has to carry the current generated by the neighboring, un-

shadowed, cells[40–45,59–61]. The underlying cause has been identified as the trap-assisted tunneling of holes through the ETL, that followingly create charge recombination centers in the perovskite bulk through the oxidation of halides to neutral halogens. This effect is exacerbated by the halide vacancy accumulation at the perovskite/ETL interface, which further increases band-bending[41,43].

Considering the crucial role of the ETL on the reverse bias breakdown of perovskite-based diodes, we evaluate the use of an alternative transport layer that can be vacuum-deposited and withstand high temperatures. The use of thermally-evaporated C_{60} satisfies these conditions, as it has been demonstrated that it possesses excellent thermal stability, even at temperatures exceeding 250°C.[62,63] Typically, a buffer layer, such as [6,6]-phenyl-C61-butyric acid methyl ester (PCBM), bathocuproine (BCP) and lithium fluoride (LiF), is inserted on top or below the C_{60} layer, to prevent charge accumulation and reduce non-radiative recombination losses[64,65]. However, these compounds have been associated with limiting a device's operational and thermal stability[66,67], leading to their exclusion from the present study. For this reason, we employ a single 40 nm C_{60} layer as the PePDs ETL (Sample 40C_{60} in **Fig. 1c**). Indeed, replacing TiO_2 with C_{60} has a positive impact on the reverse bias stability of the stack, with J_d remaining below 1 μA/cm^2 at even -3 V (**Fig. 2e**) when characterizing one of the devices with the lowest dark current (**Fig. S13c**). Nevertheless, the use of C_{60} also leads to significantly greater variability in the devices' response in dark conditions, as indicated by the wider spread of IQR in **Fig. 2b**, thereby limiting the overall reliability of the stack. The change of ETL does not seem to have a significant impact on the device's EQE (**Fig. S4b**).

The significant variability in device performance is surprising given the widespread use of C_{60} as an ETL in perovskite-based photodiodes. However, most studies on PeSC fabrication derive key performance metrics from J–V measurements under illumination, which do not reflect the variability observed under dark conditions (**Fig. 2c**). As a result, this variability may be overlooked or underestimated when the focus is placed solely on illuminated performance. We further postulate that the increased variability could stem from the absence of a buffer layer (such as BCP, PCBM, or LiF), which is typically present in comparable studies. Additionally, we believe that the large spread of the J-V curves in dark conditions is also related to the inherently small grain size of thermally evaporated perovskite. To further explore this claim, we compare the device performance of two PePDs, one that employs an as-deposited $CsPbI_2Br$ layer (**Fig. S6a**) and another with a flash-annealed (300 °C) $CsPbI_2Br$ layer (**Fig. S6b**). The as-deposited perovskite shows particularly small grain sizes, in the range of 30 – 40 nm, while the grains for the annealed state display a broad distribution of sizes, between 100 and 800 nm[49]. This increase in the perovskite's grains corresponds to a reduction of not only the median J_d but also of the IQR, even though the spread remains notable (**Fig. S6c**). This suggests that a high density of grain boundaries contributes to the variability. Thermally evaporated perovskites possess inherently smaller grains compared to their solution processed counterparts, owing to the large amount of nucleation points that arise during the initial stages of the deposition[23]. For comparison, previous studies on the use of solution-processed $CsPbI_2Br$ films have reported the attainment of perovskites with consistent grain size in the micrometer scale[68]. Lastly, in order to evaluate the impact of the thickness of the C_{60} layer on the variability of J-Vs in dark conditions we fabricate two additional samples, with 60 nm (**Fig. S7a**) and 80 nm (**Fig. S7b**) of C_{60} as the device's ETL. Increasing the thickness of the C_{60} layer has a positive impact on reducing the median J_d and the spread of the dark J-V curves, nonetheless the variability is still considerably larger compared to the 40TiO_2 samples.

Considering the complimentary advantages of using TiO_2 and C_{60} as the ETL in the PePD's performance, in terms of yield and reverse bias stability, we explore the use of a C_{60}-TiO_2 bilayer configuration through the fabrication of two additional stacks, one that employs 10 nm of C_{60} and 30 nm of TiO_2 (Sample 10C_{60}-30TiO_2 in **Fig. S8a**) and another one with 20 nm of C_{60} and 20 nm of TiO_2 (Sample 20C_{60}-20TiO_2 in **Fig. 1d**). The results for sample 10C_{60}-30TiO_2, shown in **Fig. S8b-f**, include the dynamic and static J-V curves, as well as the EQE spectra. It is evident that the inclusion of a TiO_2 layer between C_{60} and the metal contact is drastically reducing the variability in device performance, nevertheless this configuration is still not able to prevent the reverse bias breakdown. This is not the case for sample 20C_{60}-20TiO_2, whose dynamic and static J-V scans are shown in **Fig. 2c** and **Fig. 2f**, respectively. Indeed, this combination is mitigating the disadvantages of all previous samples, achieving

excellent yield in device performance (the discrete J-V scans of all devices are shown in **Fig. S3d**), as well as improved stability under reverse bias. Specifically, J_d remains below 0.5 μA/cm^2 when the device is biased at -2 V for 300 seconds and below 2 μA/cm^2 at -3 V for the same duration. Furthermore, no signs of breakdown occur when biasing the device at -2 V for 60 minutes (**Fig. S9**). These results suggest that a minimum thickness of C_{60} is required to maintain the stability of the diode under prolonged reverse bias. **Fig. S4c** shows the device's EQE spectra. Even though a slight drop compared to samples $40C_{60}$ and $40TiO_2$ is observed at 0 V, the EQE saturates at -1 V with an efficiency above 70% across the entire visible range. The observed drop in EQE at 0 V may be associated with an increase in the photodiode's series resistance (R_s), as suggested by the lower forward current density observed for the $20C_{60}$–$20TiO_2$ sample. However, this increase in R_s does not appear to affect charge extraction under reverse bias conditions. As will be discussed later, the potential increase in R_s will also not affect the speed of the PePD, since the device's response time is primarily governed by its geometrical capacitance.

Besides the stability of J_d under reverse bias, it is important to evaluate the stability of the device's photo-response, as well, since a common concern with PeSCs is the loss of power conversion efficiency under continuous illumination[69–71]. For this reason, we measured the EQE of samples $40TiO_2$, $40C_{60}$, and $20C_{60}$-$20TiO_2$ as a function of time for consecutive bias steps and two different light wavelengths (430 nm and 620 nm). With the samples being illuminated from the glass side, the absorption lengths of blue (430 nm) and red (620 nm) light are expected to correspond to the HTL/perovskite and perovskite/ETL interfaces, respectively. The results are demonstrated in **Fig. S10a-c**. Even though an EQE drop is observed at 0 V for samples $40TiO_2$ and $20C_{60}$-$20TiO_2$ when illuminated by the 620 nm light source, the photo-response remains almost completely stable for all samples as soon as we increase the reverse bias to -1 V. This is true even for sample $40TiO_2$ which should already be undergoing a breakdown at -2V. This indicates that the breakdown current (generated and saturated by the recombination of electrons and holes that are injected from the HTL and ETL side, respectively) is still two orders of magnitude lower than the photocurrent and thus does not hinder the extraction of the photogenerated carriers. As a result, the different PePDs will share a similar responsivity (R), considering the similar levels of EQE (**Figure 3a**), while their specific detectivity (D*) will be mainly determined by their reverse bias stability in dark conditions (**Figure 3b**). For example, when comparing the specific detectivity of samples $40TiO_2$ and $20C_{60}$-$20TiO_2$ under 620 nm illumination after biasing at -2 V for 300 seconds, a one-order-of-magnitude difference is observed. D*, which is calculated according to the process described in the experimental section, is equal to 8.8×10^{10} Jones and 8.8×10^{11} Jones for the $40TiO_2$ and $20C_{60}$-$20TiO_2$ samples, respectively.

The analysis of the PePD results with the bi-layer ETL configuration allows us to start disentangling the physical mechanisms that influence device performance. On one hand, the elimination of J_d variability with the inclusion of a TiO_2 layer indicates that the large spread observed for the $40C_{60}$ sample is likely attributed to the incomplete coverage of the perovskite film by the C_{60} layer and the consequent formation of contact pathways between the metal conductor and the perovskite layer[48,72]. On the other hand, the mitigation of reverse bias breakdown with the inclusion of a fullerene layer between the perovskite and TiO_2 suggests that attention should be directed toward the perovskite/ETL interface, considering that a defect-rich interface may introduce trap states that facilitate hole tunneling under reverse bias. Previous reports on the reverse bias stability of PeSCs emphasized the inclusion of a high-bandgap metal oxide between the ETL and the metal contact to reduce the hole injection rate under reverse bias[40,45]. However, in our case, the breaking down mechanism is exacerbated rather than ameliorated with the use of TiO_2, alluding that the focus should be shifted to the perovskite/ETL interface quality and not on the hole-blocking properties of the ETL.

To further investigate these hypotheses, we evaluate the elemental maps of samples $40TiO_2$, $40C_{60}$, and $20C_{60}$-$20TiO_2$, which are shown in **Fig. 4a-c**. A dashed line is drawn to indicate the start of the perovskite layer, having as a reference the onset of the Pb signal. Contrary to sample $40TiO_2$, sample $40C_{60}$ displays a stronger overlap between the Al and perovskite (Cs, Pb, I, Br) signal, further supporting the claim of incomplete surface coverage by the C_{60} layer and the creation of metallic shorts. On the

other hand, the EDS map of sample 40TiO_2 reveals that even though the Al signal is contained away from the perovskite layer, the detection of Cs signal is starting much earlier compared to Pb, I, and Br, pointing out a significantly altered stoichiometry at the interface. Such a drastic change in the surface stoichiometry of the 40TiO_2 sample could be the culprit for increased inter-bandgap states that facilitate hole tunneling under reverse bias[73–75]. Lastly, the elemental analysis of sample 20C_{60}-20TiO_2 further supports the claim that the introduction of a C_{60} layer between the perovskite and TiO_2 is helping preserve the perovskite's surface stoichiometry since the diffusion of Cs in the ETL is significantly reduced (albeit not eliminated). As a result, in the bi-layer configuration the perovskite/ETL interface quality and charge extraction dynamics are primarily dominated by the properties of the C_{60} layer, while the TiO_2 layer is mainly used to improve the device performance yield through an elimination of the Al impact on the underlying stack. The quality of the ETL/Al interface can be visually evaluated in **Fig. S2**, where the boundary between C_{60} and Al appears vague and fuzzy, while the boundary between TiO_2 and Al is sharp and well defined.

Next, transient photocurrent (TPC) measurements are performed to gain deeper insights into the improvements in interface quality with increasing C_{60} layer thickness. Specifically, two different light sources, a standard white light source and a monochromatic red light source (λ = 625 nm), are utilized, the irradiance of which was adjusted to yield a total intensity of 44.5 mW/cm^2 and 22.5 mW/cm^2, respectively (**Fig. S11a** and **Fig. S11b**). The results for the four variations of the device stack are shown in **Fig. 5a-d**. For each sample and light source, the TPC response was measured at biases of -1 V and -2 V, with all curves normalized relative to the response at -2 V. Starting with the 40TiO_2 sample biased at -1 V, the photocurrent is reaching a transient peak, before it starts decaying to a lower value. This behavior is evident for both types of illumination, though it is more pronounced when a red light source is used. The amplitude of the photocurrent peak under red light illumination is decreased for the 10C_{60}-30TiO_2 sample, and almost completely minimized for the 20C_{60}-20TiO_2 and 40C_{60} samples. Such kind of transient phenomena were previously associated with the non-ideal charge extraction and carrier accumulation at an interface[76–78]. Specifically, McNeill et al. argued that the trapping of electrons near the anode leads to a local reduction of the electric field via the generation of a space-charge region, which in turn limits charge separation and promotes recombination[78]. To further investigate the origin of the overshooting for the 40TiO_2 sample at -1 V and its dependence on the type of illumination, we simulated the charge generation rate across the perovskite layer using the transfer matrix algorithm [79]. The transfer matrix method relies on the assumption that the layers of the diode stack are homogenous, isotropic, and flat, using their thickness and optical constants as an input. As a result, the accuracy of the transfer matrix simulation relies on the fabrication of photodiodes with low interfacial roughness and the accurate determination of the optical constants of each layer. These constants are typically obtained through spectroscopic ellipsometry. **Fig. S12** presents the optical constants for all layers in the 40TiO_2 sample used in our simulation. The accuracy of the optical constants extracted for the $CsPbI_2Br$ layer was validated in our previous work[49]. Based on these inputs, we calculated the charge generation rate in the perovskite layer under red and white light illumination (**Fig. S11d**). The observed oscillatory pattern is a characteristic signature of optical interference within a cavity structure. Interestingly, the generation rate at the perovskite/ETL interface (distance = 300 nm) is similar for illumination with the red and white light source (~2×10^{21} s^{-1}cm^{-3}). Therefore, considering that the rate of charge trapping is directly proportional to the density of free carriers[77] , we could reasonably assume similar levels of trapped-charge accumulation at the perovskite/TiO_2 interface for illumination with red and white light, leading to the formation of a space-charge region of similar width. However, the inefficient charge separation and extraction close to the perovskite/ETL interface is less detrimental when the sample is illuminated with white light, since a significantly larger number of carriers is generated close to the HTL/perovskite interface (distance = 0 – 100 nm in **Fig. S11d**). This is the reason why the overshooting peak is more dominant for illumination with the red light. When the bias is increased at -2 V, the overshoot peak disappears, indicating a faster and more efficient extraction of generated carriers, which prevents the formation of a space-charge region. Consequently, the diminished overshooting peak observed with increasing C_{60} layer thickness can be attributed to a reduction in the density of interface trap states. It has to be highlighted that despite the steady-state photocurrent for sample 40TiO_2 being almost half at -1 V compared to -2 V (**Fig. 5a**), the EQE response of the sample is close to 70% for both bias steps under red light illumination (620 nm) in **Fig. S10a**. This is mainly attributed to the

significantly lower intensity of the EQE light source (approximately one order of magnitude lower, <3 mW/cm^2) and the fact that the trapped-charge accumulation is directly proportional to it[77,78].

Through the TPC measurements, it is possible to extract additional information about the impact of the ETL on the response speed of the devices, an important figure of merit for photodetectors. **Fig. 6a** shows an overlay comparison of the response speed for all samples under white light illumination, biased at -2 V. A trend of increasing response speed with increasing thickness of the C_{60} layer is evident. We can calculate the response speed of each diode using the 10%-90% rule, as shown in **Fig. S13**. **Fig. 6b** highlights the decrease in the signal's rise time with increasing C_{60} thickness. To further investigate the origin of this correlation and taking into account that for devices with area in the range of cm^2 the response speed is dominated by the RC constant[20], we measure the devices' capacitance as a function of frequency at 0 and -2 V (**Fig. S14**). The capacitance of sample 40TiO_2 is collapsing for lower frequencies at -2 V (**Fig. S14b**), a direct aftermath of its reverse bias breakdown. Nonetheless, for frequencies above 10 Hz, the capacitance at 0 V and –2 V is identical across all samples. The capacitance depends on the electrode area and dielectric thickness, however the area is fixed and defined by the opening of the metal mask. Thus, the constant capacitance value indicates that that the dielectric width does not change with increasing reverse bias, a condition that is only met when the capacitor is fully depleted at 0 V. This is a common consideration for perovskite-based diodes, as the perovskite layer is nearly intrinsic, and its entire thickness can be fully depleted by the built-in potential established by the contacts[80]. In conclusion, **Fig. S14** confirms that the increase in speed is not related to an extension of the depletion region within the perovskite itself[81]. **Fig. 6c** provides an overlay comparison of the capacitance for all samples at 0 V, which highlights that the capacitance of the stack at moderate frequencies is inversely proportional to the thickness of the C_{60} layer. It has been previously numerically shown that, due to its relatively low doping density, the depletion region can extend into the C_{60} layer[82], as well, which could potentially explain the trend of increasing speed we observe. Considering that for the 40TiO_2 sample only the perovskite layer is depleted, and using the equation $C_{pvkt} = \frac{\varepsilon_r \varepsilon_0 A}{d}$ (where ε_r is the relative permittivity of the perovskite, ε_0 is the vacuum permittivity, A is the device area, and d is the thickness of the perovskite layer), we extract $\varepsilon_r = 26.5$. The parameters used for the calculation are shown in **Table 1**. To corroborate this measurement, we additionally fabricate a metal-oxide-semiconductor (MOS) capacitor, using a heavily p-doped silicon substrate with 100 nm of thermally grown silicon oxide (SiO_2). The structure of the capacitor and its C-f characteristic are shown in **Fig. S15a** and **Fig. S15b**, respectively. In this case, the equivalent capacitance will be given from equation $\frac{1}{C_{eq}} = \frac{1}{C_{ox}} + \frac{1}{C_{pvkt}}$. Using the values indicated in **Table 2**, we extract $\varepsilon_r = 26.9$, which agrees with the value calculated for the 40TiO_2 sample. As the last step, we calculate the equivalent capacitance for all stacks with C_{60} (considering that the C_{60} layer is fully depleted) and compare it with the measured values in **Fig. 6d**. Measured and calculated capacitance values are in excellent agreement, confirming our hypothesis that the increase in the photodiode's response speed with increasing thickness of the C_{60} layer is attributed to a reduction of the RC constant through the depletion of the C_{60} layer[81].

This finding gives the motivation to fabricate an additional ETL stack consisting of 40 nm of C_{60} and 20 nm of TiO_2 as the ETL. The J-V response, EQE spectra, and rise time of this stack are shown in **Fig. S16a-c**. Indeed, the rise time is further increased compared to the 20C_{60}20TiO_2 stack (going from 2.17 µs to 1.96 µs for the same device area of 0.125 cm^2) and approximates the response time of the 40C_{60} stack (1.9 µs). However, when looking at the EQE spectra, the response does no longer saturate at -1 V, and it remains below 70% even at -2 V. This finding is consistent with previous reports that show a drop in the PCE of PeSCs when the C_{60} layer thickness crosses a specific threshold[83]. Therefore, depending on the application, a compromise between speed and carrier extraction efficiency could be made. Of course, this compromise can be avoided by scaling down the diode's area, which in turn minimizes the capacitance. To demonstrate this, we decrease the contact area of sample 40C_{60} from 0.125 cm^2 to 0.075 cm^2 and 0.025 cm^2. The reduction in the device's capacitance is illustrated in **Fig. S17a** and the consequent increase in response speed is shown in **Fig. S17b**. The extracted rise time as a function of area is illustrated in **Fig. S17c**, demonstrating a linear dependence. The 1 µs rise time for the device

with 0.025 cm^2 area is near the detection limit of the setup; however, sub-μs speeds can be projected for further scaled-down pixels.

Finally, in order to evaluate the performance of our PePDs relative to previous literature reports that employ thermally evaporated inorganic perovskites ($CsPbX_3$, where X = I, Br, Cl, or their combinations) for the fabrication of photodiodes, we compile a summary of the most characteristic parameters in **Table S1**. Among the available reports, only Yang et al. examine the PePD's performance at -2 V, where the diode operates in photoconductive gain mode (EQE > 100%), resulting in unusually high responsivity and specific detectivity[30]. The remaining studies either focus on "self-powered" diodes (operating at 0 V) or apply only a moderate bias of -0.5 V. Our work uniquely demonstrates reliable operation at -2 V, achieving the lowest J_d in this bias range while maintaining one of the fastest response times—all without compromising the device's responsivity.

4. Conclusions

In conclusion, with a focus on p-i-n, vacuum-deposited, all-inorganic PePDs, we have demonstrated that the careful tuning of the ETL is necessary to ensure reliable operation. The study mainly focused on the use of thermally evaporated C_{60} and e-beam deposited TiO_2 as the diode's ETLs. The use of C_{60} was associated with large variability in device performance, which was attributed to the diffusion of the Al top contact into the perovskite layer, as revealed through TEM-EDS. The same measurement indicated that the deposition of TiO_2 directly on top of the perovskite leads to significant changes in the perovskite's surface stoichiometry, which in turn creates defect states that promote the breakdown of the PePD under reverse bias. Additional TPC measurements using both white and red light sources, allowing the precise control over the absorption depth and profile, further confirmed the increased interface trap states in devices with TiO_2. Eventually, it was shown that the sequential deposition of C_{60} and TiO_2 for the device's ETL is sufficient to mitigate the challenges arising from using each layer separately. Our findings demonstrate that the thickness of the C_{60} layer in the bilayer ETL is critical for enhancing charge extraction speed by extending the diode's depletion width. However, while a thicker C_{60} layer improves extraction speed, an excessive increase begins to limit quantum efficiency. This drawback can be mitigated by further reducing the detector's area. We believe that this study strengthens the foundations of high-temperature tolerant, scalable and efficient PePDs, pushing the technology closer to the standards of complementary metal-oxide semiconductor (CMOS) applications.

5. Experimental Section

5.1 Perovskite Deposition

$CsPbI_2Br$ perovskite thin films were deposited via thermal co-evaporation using a Kurt J. Lesker SPECTROS system. Two diametrically opposed sources were used for the evaporation of CsBr (abcr, ultra dry; 99.9%) and PbI_2 (TCI Chemicals, >98%) powders. For each deposition, the crucibles would be emptied and re-loaded with ~1 g of fresh material. The deposition rate of each source was individually monitored by a designated QCM sensor. Prior to the co-evaporations, the tooling factor of sensor was calibrated by separately depositing CsBr and PbI_2 films on a Si/SiO_2 substrate and measuring the respective precursor thickness with ex situ ellipsometry (RC2 J.A. Woolam). For stoichiometric films, the rate ratio of two precursors A and B should be equal to $\frac{evap.rate\ (A)}{evap.rate\ (B)} = \frac{molar\ mass\ (A)\ /\ density\ (A)}{molar\ mass\ (B)\ /\ density\ (B)}$. Similarly to our previous work, we aimed for 1.05:1.00 CsBr to PbI_2 ratio and a cumulative evaporation rate of ~0.8 Å/s. The base pressure of the chamber was below 10^{-6} Torr. The duration of the deposition was tuned to obtain $CsPbI_2Br$ films with a nominal thickness of 300 nm. The deposition was initiated when the rates of both sources were stabilized at their set value by removing the global shutter. The deposition rate of each source was maintained throughout the deposition via an automatic adjustment of their temperature. The substrate holder, which can be loaded with up to nine 3×3 cm^2 substrates, was constantly rotating to ensure uniform deposition, while being kept at room temperature.

5.2 Device Fabrication

For the fabrication of photodetector diodes, 3×3 cm^2 glass substrates, pre-patterned with ITO stripes (15 Ω, Colorado Concept Coatings), were used. For their cleaning, the substrates were placed in an ultrasonic bath at 50°C, being sequentially submerged in water comprising Extran as surfactant, deionized water, acetone and isopropanol. Each cleaning step lasted 10 minutes. After being thoroughly dried with a nitrogen gun, the substrates were transferred into a high-vacuum chamber (Nebula system, Angstrom Engineering Inc.) for the deposition of 15 nm thick NiO_x films via reactive sputtering of a metallic nickel target using oxygen plasma (base pressure 10^{-7}-10^{-8} Torr). The NiO_x-coated substrates were then annealed in open air for 5 minutes at 300°C. Afterwards, ~300 nm thick $CsPbI_2Br$ films were deposited following the process described above. Post perovskite deposition, the substrates were flash annealed (approximately 5 sec) at 300°C in a nitrogen-filled glovebox. For the deposition of ETLs and Al contacts, a high-vacuum evaporation system was used (Angstrom Engineering Inc.) C_{60} was thermally evaporated at a rate of 0.2 Å/s. TiO_2 was deposited via e-beam evaporation at a similar rate of 0.2 Å/s. During TiO_2 deposition, an oxygen flow of 9 sccm was introduced in the chamber to compensate vacancies created during deposition[55]. Lastly, 100 nm of Al contacts were deposited via thermal evaporation at a rate of ~0.4 - 0.5 Å/s, using shadow masks for defining the contact area of 12 devices on the same substrate.

For the fabrication of MIS capacitors, 3×3 cm^2 coupons from a Si wafer (p-type, 0.005 – 0.010 Ohm-cm) with 100 nm of thermally grown SiO2, and an Al back contact (500 nm) were used. These substrates were also cleaned in an ultrasonic path, using acetone and isopropanol. The perovskite layer was then deposited and annealed in the same way as described above. Au contacts of various sizes were deposited via thermal evaporation using a high-vacuum evaporation system (Angstrom Engineering Inc.).

5.3 Device Characterization

All measurements were performed in N_2-filled gloveboxes. The current density – voltage (J-V) characteristics of the PePDs were recorded using a Keithley 2602A source-measure unit. The dynamic scans were performed using medium integration time, 0.01 V bias step and 0.01 s delay with a -2 V to 2 V direction. The J-V curves under illumination were recorded with similar settings under 1 sun illumination (100 mW/cm^3 - AM 1.5G). The device's EQE as a function of wavelength, bias, and time was recorded with a Stanford Research System model SR830 lock-in amplifier unit coupled with a monochromator and a 150 W halogen lamp (OSRAM HLX 64633). A low-noise current preamplifier (Stanford Research System) was used to amplify the signal. A Si photodiode with a known spectral response was used for calibration. The capacitance and transient photocurrent measurements were performed using a Paios all-in-one system by Fluxim. Two different light emitting diodes were used for the device illumination with white (Cree LED XPGWHT-01-0000-00EE5) and red light (WL-SMDC SMT Mono-color Ceramic LED Waterclear 150353RS74500). For the estimation of the PePD's specific detectivity, it was considered that the shot noise is the main contributor to the noise equivalent power in the dark, and that the contributions of Johnson and flick noise are negligible[35]. Therefore, the formula $D^* = R/(2eJ_d)^{1/2}$ ($\frac{cm\ Hz^{\frac{1}{2}}}{W}$ *or* Jones) was used, where R is the device's responsivity, e is the electron charge, and J_d is the dark current density (obtained through steady-state measurements). In turn, the device's responsivity was estimated through the formula $R = \frac{e}{hc/\lambda} \times EQE$, where h is Planck's constant, c is the speed of light, and λ is the incoming wavelength.

Transmission Electron Microscopy: For local analysis of the structure and composition with transmission electron microscope (TEM), cross-sections (70 nm thickness) of the devices were prepared using focused ion beam (FIB) on FEI Helios Nanolab 650. Prior to FIB cutting, Pt layer was deposited as protective layer. Prepared FIB lamellas were subjected to high angle annular dark field scanning transmission electron microscopy (HAADF-STEM) imaging. The images were acquired in a low-dose (<1500 e-/Å2) regime using a probe-corrected Thermo FisherTitan Themis Z microscope operated at 300 kV with a probe semi-convergence angle of 21 mrad and equipped with a 4 quadrant Super X detector for energy dispersive x-ray spectroscopy (EDS). Acquisition time for EDS measurements was around 1200 s.

Supporting Information:

- Ambient phase stability and AFM scans of $CsPbI_3$ films with various % of Br doping; STEM cross-section of PePDs; Discrete JV scans for 12 devices on the same substrate; EQE as a function of wavelength; Reversibility of reverse breakdown mechanism; Impact of annealing on grain morphology and JV characteristics for PePD with C_{60}; Impact of C_{60} thickness on JV characteristics; Complete characterization of PePD with 10 nm of C_{60} and 30 nm of TiO_2; Effect of prolonged reverse bias on sample $20C_{60}$-$20TiO_2$; EQE as a function of time; Illumination profiles for TPC measurements and transfer matrix simulation results; Optical constants of all PePD layers; Response speed of PePDs under transient illumination; Capacitance as function of frequency for all PePDs; Schematic and capacitance profile of MOS structure; Characterization of sample with 40 nm of C_{60} and 20 nm of TiO_2 as the ETL; Impact of scaling down detector area on capacitance and response speed; Table for benchmarking PePD performance against other photodiodes with inorganic and vacuum-deposited perovskite

Acknowledgement:
We acknowledge the financial support from the Fund for Scientific Research Flanders (FWO) under Project number S004322N (GigaPixel). I.S. acknowledges financial support from the Research Foundation – Flanders (FWO) through a doctoral fellowship (FWO-SB Grant No. 1SHA024N).

Data Availability:
All the data that support the findings of this study are available from the corresponding authors upon reasonable request.

Author Information:

Corresponding Author

Athina Papadopoulou[1,2*]
E-mail: athina.papadopoulou@imec.be

Maria Isabel Pintor-Monroy[1*]
E-mail: isabel.pintormonroy@imec.be

[1]imec, Kapeldreef 75, 3001 Leuven, Belgium
[2]Department of Electrical Engineering (ESAT), KU Leuven, Kasteelpark Arenberg 10, 3001 Leuven, Belgium

6. Bibliography

(1) Aydin, E.; Allen, T. G.; Bastiani, M. De; Razzaq, A.; Xu, L.; Ugur, E.; Liu, J.; De Wolf, S. Pathways toward Commercial Perovskite/Silicon Tandem Photovoltaics. *Science (1979)* **2024**, *383* (6679), 1–13. https://doi.org/10.1126/science.adh3849.

(2) Lim, J.; Park, N. G.; Il Seok, S.; Saliba, M. All-Perovskite Tandem Solar Cells: From Fundamentals to Technological Progress. *Energy Environ Sci* **2024**, *17* (13), 4390–4425. https://doi.org/10.1039/d3ee03638c.

(3) Wu, D.; Xu, Y.; Zhou, H.; Feng, X.; Zhang, J.; Pan, X.; Gao, Z.; Wang, R.; Ma, G.; Tao, L.; Wang, H.; Duan, J.; Wan, H.; Zhang, J.; Shen, L.; Wang, H.; Zhai, T. Ultrasensitive, Flexible Perovskite Nanowire Photodetectors with Long-Term

Stability Exceeding 5000 h. *InfoMat* **2022**, *4* (9), e12320. https://doi.org/10.1002/inf2.12320.
(4) Zhou, H.; Song, Z.; Grice, C. R.; Chen, C.; Zhang, J.; Zhu, Y.; Liu, R.; Wang, H.; Yan, Y. Self-Powered CsPbBr3 Nanowire Photodetector with a Vertical Structure. *Nano Energy* **2018**, *53*, 880–886. https://doi.org/10.1016/j.nanoen.2018.09.040.
(5) Tian, W.; Zhou, H.; Li, L. Hybrid Organic–Inorganic Perovskite Photodetectors. *Small* **2017**, *13* (41), 1702107. https://doi.org/10.1002/smll.201702107.
(6) Li, L.; Ye, S.; Qu, J.; Zhou, F.; Song, J.; Shen, G.; Li, L.; Ye, S.; Qu, J.; Zhou, F.; Song, J.; Shen, G. Recent Advances in Perovskite Photodetectors for Image Sensing. *Small* **2021**, *17* (18), 2005606. https://doi.org/10.1002/smll.202005606.
(7) Li, G.; Wang, Y.; Huang, L.; Sun, W. Research Progress of High-Sensitivity Perovskite Photodetectors: A Review of Photodetectors: Noise, Structure, and Materials. *ACS Appl Electron Mater* **2022**, *4* (4), 1485–1505. https://doi.org/10.1021/acsaelm.1c01349.
(8) Fakharuddin, A.; Gangishetty, M. K.; Abdi-Jalebi, M.; Chin, S. H.; bin Mohd Yusoff, A. R.; Congreve, D. N.; Tress, W.; Deschler, F.; Vasilopoulou, M.; Bolink, H. J. Perovskite Light-Emitting Diodes. *Nature Electronics 2022 5:4* **2022**, *5* (4), 203–216. https://doi.org/10.1038/S41928-022-00745-7.
(9) Sun, Y.; Ge, L.; Dai, L.; Cho, C.; Ferrer Orri, J.; Ji, K.; Zelewski, S. J.; Liu, Y.; Mirabelli, A. J.; Zhang, Y.; Huang, J. Y.; Wang, Y.; Gong, K.; Lai, M. C.; Zhang, L.; Yang, D.; Lin, J.; Tennyson, E. M.; Ducati, C.; Stranks, S. D.; Cui, L. S.; Greenham, N. C. Bright and Stable Perovskite Light-Emitting Diodes in the near-Infrared Range. *Nature 2023 615:7954* **2023**, *615* (7954), 830–835. https://doi.org/10.1038/S41586-023-05792-4.
(10) Goldberg, I.; Elkhouly, K.; Annavarapu, N.; Hamdad, S.; Gonzalez, M. C.; Genoe, J.; Gehlhaar, R.; Heremans, P. Toward Thin-Film Laser Diodes with Metal Halide Perovskites. *Advanced Materials* **2024**, *36* (40), 2314193. https://doi.org/10.1002/adma.202314193.
(11) Lei, L.; Dong, Q.; Gundogdu, K.; So, F.; Lei, L.; Dong, Q.; So, F.; Gundogdu, K. Metal Halide Perovskites for Laser Applications. *Adv Funct Mater* **2021**, *31* (16), 2010144. https://doi.org/10.1002/adfm.202010144.
(12) Mei, L.; Huang, R.; Shen, C.; Hu, J.; Wang, P.; Xu, Z.; Huang, Z.; Zhu, L. Hybrid Halide Perovskite-Based Near-Infrared Photodetectors and Imaging Arrays. *Adv Opt Mater* **2022**, *10* (9), 2102656. https://doi.org/10.1002/ADOM.202102656.
(13) Deumel, S.; van Breemen, A.; Gelinck, G.; Peeters, B.; Maas, J.; Verbeek, R.; Shanmugam, S.; Akkerman, H.; Meulenkamp, E.; Huerdler, J. E.; Acharya, M.; García-Batlle, M.; Almora, O.; Guerrero, A.; Garcia-Belmonte, G.; Heiss, W.; Schmidt, O.; Tedde, S. F. High-Sensitivity High-Resolution X-Ray Imaging with Soft-Sintered Metal Halide Perovskites. *Nature Electronics 2021 4:9* **2021**, *4* (9), 681–688. https://doi.org/10.1038/s41928-021-00644-3.
(14) Li, L.; Fang, Y.; Yang, D. Interlayer-Assisted Growth of Si-Based All-Inorganic Perovskite Films via Chemical Vapor Deposition for Sensitive and Stable X-ray Detection. *J. Phys. Chem. Lett* **2022**, *4* (13), 5441–5450. https://doi.org/10.1021/acs.jpclett.2c01389.
(15) Lai, P.-T.; Lin, H.-C.; Chuang, Y.-T.; Chen, C.-Y.; Cheng, W.-K.; Tan, G.-H.; Hsu, B.-W.; Yang, L.; Lou, S.-C.; Chien, L.-J.; Wang, H.-W.; Lin, H.-W. All-Vacuum-Deposited Perovskite X-Ray Detector with a Record-High Self-Powered Sensitivity of 1.2 C Gy-1 Cm-3. *ACS Appl. Mater. Interfaces* **2022**, 19795–19805. https://doi.org/10.1021/acsami.2c03114.

(16) Li, W.; Xu, Y.; Peng, J.; Li, R.; Song, J.; Huang, H.; Cui, L.; Lin, Q. Evaporated Perovskite Thick Junctions for X-Ray Detection. *ACS Appl. Mater. Interfaces* **2021**, *13* (2), 2971–2978. https://doi.org/10.1021/acsami.0c20973.
(17) Wu, W.; Zhang, J.; Liu, C.; Zhang, J.; Lai, H.; Hu, Z.; Zhou, H. Spontaneous Cooling Enables High-Quality Perovskite Wafers for High-Sensitivity X-Ray Detectors with a Low-Detection Limit. *Advanced Science* **2024**, *11* (46), 2410303. https://doi.org/10.1002/advs.202410303.
(18) Green, M. A.; Ho-Baillie, A.; Snaith, H. J. The Emergence of Perovskite Solar Cells. *Nature Photonics 2014 8:7* **2014**, *8* (7), 506–514. https://doi.org/10.1038/nphoton.2014.134.
(19) Zhao, Y.; Li, C.; Shen, L. Recent Advances on Organic-Inorganic Hybrid Perovskite Photodetectors with Fast Response. *InfoMat* **2019**, *1* (2), 164–182. https://doi.org/10.1002/inf2.12010.
(20) Song, W.; Kang, J.; Elkhouly, K.; Hamdad, S.; Zhang, X.; Pintor Monroy, M. I.; Siddik, A. B.; Carolan, P.; Subramaniam, S.; Kuang, Y.; De Roose, F.; Vandenplas, E.; Chandrasekaran, N.; Kim, J. H.; Gehlhaar, R.; Kim, S. J.; Lee, J.; Genoe, J. Halide Perovskite Photodiode Integrated CMOS Imager. *ACS Nano* **2024**, *18*, 35532. https://doi.org/10.1021/acsnano.4c13136.
(21) Wang, X.; Ning, H.; Hu, G.; Li, Y.; Xie, Y.; Lin, J.; Zhuo, C.; Bodepudi, S. C.; Wang, Y.; Yu, B.; Xu, Y. A Monolithically Integrated 640 × 512 CMOS-Perovskite Image Sensor. *2024 IEEE European Solid-State Electronics Research Conference (ESSERC)* **2024**, 213–216. https://doi.org/10.1109/ESSERC62670.2024.10719487.
(22) Yen, P. W.; Lin, Y. R.; Yu, S. M.; Lou, S. C.; Chuang, K. P.; Chuang, B. N.; Chiou, Y. C.; Hsieh, C. C. A Hybrid CMOS-Imager with Perovskites as Photoactive Layer. In *Proceedings of IEEE Sensors*; Institute of Electrical and Electronics Engineers Inc., 2016; Vol. 0. https://doi.org/10.1109/ICSENS.2016.7808480.
(23) Vaynzof, Y. The Future of Perovskite Photovoltaics-Thermal Evaporation or Solution Processing? *Adv. Energy Mater.* **2020**, *10*, 2003073. https://doi.org/10.1002/aenm.202003073.
(24) Saki, Z.; Byranvand, M. M.; Taghavinia, N.; Kedia, M.; Saliba, M. Solution-Processed Perovskite Thin-Films: The Journey from Lab-to Large-Scale Solar Cells. *Energy Environ. Sci* **2021**, *14*, 5690–5722. https://doi.org/10.1039/d1ee02018h.
(25) Du, P.; Wang, L.; Li, J.; Luo, J.; Ma, Y.; Tang, J.; Zhai, T. Thermal Evaporation for Halide Perovskite Optoelectronics: Fundamentals, Progress, and Outlook. *Adv Opt Mater* **2022**, *10* (4), 2101770. https://doi.org/10.1002/ADOM.202101770.
(26) Schwenzer, J. A.; Hellmann, T.; Nejand, B. A.; Hu, H.; Abzieher, T.; Schackmar, F.; Hossain, I. M.; Fassl, P.; Mayer, T.; Jaegermann, W.; Lemmer, U.; Paetzold, U. W. Thermal Stability and Cation Composition of Hybrid Organic-Inorganic Perovskites. *ACS Appl Mater Interfaces* **2021**, *13* (13), 15292–15304. https://doi.org/10.1021/acsami.1c01547.
(27) Dong, Z.; Li, W.; Wang, H.; Jiang, X.; Liu, H.; Zhu, L.; Chen, H. High-Temperature Perovskite Solar Cells. *Solar RRL* **2021**, *5* (9), 2100370. https://doi.org/10.1002/solr.202100370.
(28) Mariotti, S.; Hutter, O. S.; Phillips, L. J.; Yates, P. J.; Kundu, B.; Durose, K. Stability and Performance of CsPbI2Br Thin Films and Solar Cell Devices. *ACS Appl Mater Interfaces* **2018**, *10* (4), 3750–3760. https://doi.org/10.1021/acsami.7b14039.

(29) Li, L.; Tao, L.; Wang, L.; Li, Y.; Li, J.; Ni, Z.; Fang, Y.; Yang, D. Monolithic Integration of Perovskite Heterojunction on TFT Backplanes through Vapor Deposition for Sensitive and Stable X-Ray Imaging. *Sci Adv* **2024**, *10* (17), eadj8659. https://doi.org/10.1126/sciadv.adj8659.
(30) Yang, L.; Tsai, W. L.; Li, C. S.; Hsu, B. W.; Chen, C. Y.; Wu, C. I.; Lin, H. W. High-Quality Conformal Homogeneous All-Vacuum Deposited CsPbCl3 Thin Films and Their UV Photodiode Applications. *ACS Appl Mater Interfaces* **2019**, *11* (50), 47054–47062. https://doi.org/10.1021/acsami.9b16264.
(31) Igual-Muñoz, A. M.; Navarro-Alapont, J.; Dreessen, C.; Palazon, F.; Sessolo, M.; Bolink, H. J. Room-Temperature Vacuum Deposition of CsPbI2Br Perovskite Films from Multiple Sources and Mixed Halide Precursors. *Chemistry of Materials* **2020**, *32* (19), 8641–8652. https://doi.org/10.1021/acs.chemmater.0c03038.
(32) Jiang, S.; Hou, Z.; Zheng, X.; Wu, Q.; Yang, X.; Cai, W.; Yi, Y.; Cheng, S.; Wen, G.; Liu, X. Ultrafast Self-Powered CsPbCl3 Ultraviolet Photodetectors with Choline Chloride for Surface Passivation and Charge Transport Regulation. *J Mater Chem C Mater* **2023**, *11* (17), 5667–5679. https://doi.org/10.1039/d3tc00063j.
(33) Zhan, X.; Zhang, X.; Liu, Z.; Chen, C.; Kong, L.; Jiang, S.; Xi, S.; Liao, G.; Liu, X. Boosting the Performance of Self-Powered CsPbCl3-Based UV Photodetectors by a Sequential Vapor-Deposition Strategy and Heterojunction Engineering. *ACS Appl Mater Interfaces* **2021**, *13* (38), 45744–45757. https://doi.org/10.1021/acsami.1c15013.
(34) Bai, T.; Wang, S.; Bai, L.; Zhang, K.; Chu, C.; Yi, L. Vacuum Evaporation of High-Quality CsPbBr3 Thin Films for Efficient Light-Emitting Diodes. *Nanoscale Research Letters 2022 17:1* **2022**, *17* (1), 1–11. https://doi.org/10.1186/s11671-022-03708-1.
(35) Pintor Monroy, M. I.; Goldberg, I.; Elkhouly, K.; Georgitzikis, E.; Clinckemalie, L.; Croes, G.; Annavarapu, N.; Qiu, W.; Debroye, E.; Kuang, Y.; Roeffaers, M. B. J.; Hofkens, J.; Gehlhaar, R.; Genoe, J. All-Evaporated, All-Inorganic CsPbI3 Perovskite-Based Devices for Broad-Band Photodetector and Solar Cell Applications. *ACS Appl Electron Mater* **2021**, *3* (7), 3023–3033. https://doi.org/10.1021/ACSAELM.1C00252.
(36) Zhao, B.; Jin, S. F.; Huang, S.; Liu, N.; Ma, J. Y.; Xue, D. J.; Han, Q.; Ding, J.; Ge, Q. Q.; Feng, Y.; Hu, J. S. Thermodynamically Stable Orthorhombic γ-CsPbI3 Thin Films for High-Performance Photovoltaics. *J Am Chem Soc* **2018**, *140* (37), 11716–11725. https://doi.org/10.1021/jacs.8b06050.
(37) Steele, J. A.; Jin, H.; Dovgaliuk, I.; Berger, R. F.; Braeckevelt, T.; Yuan, H.; Martin, C.; Solano, E.; Lejaeghere, K.; Rogge, S. M. J.; Notebaert, C.; Vandezande, W.; Janssen, K. P. F.; Goderis, B.; Debroye, E.; Wang, Y. K.; Dong, Y.; Ma, D.; Saidaminov, M.; Tan, H.; Lu, Z.; Dyadkin, V.; Chernyshov, D.; Van Speybroeck, V.; Sargent, E. H.; Hofkens, J.; Roeffaers, M. B. J. Thermal Unequilibrium of Strained Black CsPbI3 Thin Films. *Science (1979)* **2019**, *365* (6454), 679–684. https://doi.org/10.1126/SCIENCE.AAX3878.
(38) Steele, J. A.; Prakasam, V.; Huang, H.; Solano, E.; Chernyshov, D.; Hofkens, J.; Roeffaers, M. B. J. Trojans That Flip the Black Phase: Impurity-Driven Stabilization and Spontaneous Strain Suppression in γ-CsPbI3 Perovskite. *J. Am. Chem. Soc* **2021**, *143*, 10500–10508. https://doi.org/10.1021/jacs.1c05046.
(39) Jin, H.; Zeng, Y. J.; Steele, J. A.; Roeffaers, M. B. J.; Hofkens, J.; Debroye, E. Phase Stabilization of Cesium Lead Iodide Perovskites for Use in Efficient

Optoelectronic Devices. *NPG Asia Materials 2024 16:1* **2024**, *16* (1), 1–18. https://doi.org/10.1038/s41427-024-00540-0.
(40) Li, N.; Shi, Z.; Fei, C.; Jiao, H.; Li, M.; Gu, H.; Harvey, S. P.; Dong, Y.; Beard, M. C.; Huang, J. Barrier Reinforcement for Enhanced Perovskite Solar Cell Stability under Reverse Bias. *Nat Energy* **2024**, 1264–1275. https://doi.org/10.1038/s41560-024-01579-7.
(41) Bertoluzzi, L.; Patel, J. B.; Bush, K. A.; Boyd, C. C.; Kerner, R. A.; O, B. C.; McGehee, M. D.; Bertoluzzi, L.; Bush, K. A.; Boyd, C. C.; Patel, J. B.; Kerner, R. A.; McGehee, M. D. Incorporating Electrochemical Halide Oxidation into Drift-Diffusion Models to Explain Performance Losses in Perovskite Solar Cells under Prolonged Reverse Bias. *Adv Energy Mater* **2021**, *11* (10), 2002614. https://doi.org/10.1002/AENM.202002614.
(42) Wang, C.; Huang, L.; Zhou, Y.; Guo, Y.; Liang, K.; Wang, T.; Liu, X.; Zhang, J.; Hu, Z.; Zhu, Y.; Wang, C.; Huang, L.; Zhou, Y.; Guo, Y.; Liang, K.; Wang, T.; Liu, X.; Zhang, J.; Hu, Z.; Zhu, Y. Perovskite Solar Cells in the Shadow: Understanding the Mechanism of Reverse-Bias Behavior toward Suppressed Reverse-Bias Breakdown and Reverse-Bias Induced Degradation. *Adv Energy Mater* **2023**, *13* (9), 2203596. https://doi.org/10.1002/AENM.202203596.
(43) Bowring, A. R.; Bertoluzzi, L.; O'Regan, B. C.; McGehee, M. D. Reverse Bias Behavior of Halide Perovskite Solar Cells. *Adv Energy Mater* **2018**, *8* (8), 1702365. https://doi.org/10.1002/aenm.201702365.
(44) Razera, R. A. Z.; Jacobs, D. A.; Fu, F.; Fiala, P.; Dussouillez, M.; Sahli, F.; Yang, T. C. J.; Ding, L.; Walter, A.; Feil, A. F.; Boudinov, H. I.; Nicolay, S.; Ballif, C.; Jeangros, Q. Instability of P-i-n Perovskite Solar Cells under Reverse Bias. *J. Mater. Chem. A* **2020**, *8*, 242. https://doi.org/10.1039/c9ta12032g.
(45) Ni, Z.; Jiao, H.; Fei, C.; Gu, H.; Xu, S.; Yu, Z.; Yang, G.; Deng, Y.; Jiang, Q.; Liu, Y.; Yan, Y.; Huang, J. Evolution of Defects during the Degradation of Metal Halide Perovskite Solar Cells under Reverse Bias and Illumination. *Nature Energy 2021 7:1* **2021**, *7* (1), 65–73. https://doi.org/10.1038/S41560-021-00949-9.
(46) Martínez-Goyeneche, L.; Ollearo, R.; Bordoni, C.; Ciavatti, A.; van Breemen, A. J. J. M.; Gelinck, G. H.; Fraboni, B.; Tordera, D.; Sessolo, M. Vacuum-Deposited Perovskite Photodiodes for Visible and X-Ray Photon Detection. *Adv Opt Mater* **2024**, *12* (20), 2400464. https://doi.org/10.1002/adom.202400464.
(47) Ollearo, R.; Wang, J.; Dyson, M. J.; Weijtens, C. H. L.; Fattori, M.; van Gorkom, B. T.; van Breemen, A. J. J. M.; Meskers, S. C. J.; Janssen, R. A. J.; Gelinck, G. H. Ultralow Dark Current in Near-Infrared Perovskite Photodiodes by Reducing Charge Injection and Interfacial Charge Generation. *Nature Communications 2021 12:1* **2021**, *12* (1), 1–9. https://doi.org/10.1038/s41467-021-27565-1.
(48) Lin, Q.; Armin, A.; Lyons, D. M.; Burn, P. L.; Meredith, P.; Lin, Q.; Armin, A.; Lyons, D. M.; Burn, P. L.; Meredith, P. Low Noise, IR-Blind Organohalide Perovskite Photodiodes for Visible Light Detection and Imaging. *Advanced Materials* **2015**, *27* (12), 2060–2064. https://doi.org/10.1002/ADMA.201405171.
(49) Papadopoulou, A.; Saha, R. A.; Pintor-Monroy, M. I.; Song, W.; Lieberman, I.; Solano, E.; Roeffaers, M. B. J.; Gehlhaar, R.; Genoe, J. In Situ Annealing Effect on Thermally Co-Evaporated CsPbI2Br Thin Films Studied via Spectroscopic Ellipsometry. *ACS Appl Mater Interfaces* **2024**, *16* (36), 47889–47901. https://doi.org/10.1021/acsami.4c09283.
(50) Siddik, A. B.; Georgitzikis, E.; Hermans, Y.; Kang, J.; Kim, J. H.; Pejovic, V.; Lieberman, I.; Malinowski, P. E.; Kadashchuk, A.; Genoe, J.; Conard, T.; Cheyns,

D.; Heremans, P. Interface-Engineered Organic Near-Infrared Photodetector for Imaging Applications. *ACS Appl Mater Interfaces* **2023**, *15* (25), 30534–30542. https://doi.org/doi.org/10.1021/acsami.3c03708.

(51) Siddik, A. B.; Georgitzikis, E.; Song, W.; Papadopoulou, A.; Zaman, A. U.; Lim, M. J.; Pejovic, V.; Lieberman, I.; Malinowski, P. E.; Genoe, J.; Conard, T.; Cheyns, D.; Heremans, P. PbS and InAs Quantum-Dot Thin Films for Short-Wave Infrared Detectors. *ACS Appl Nano Mater* **2024**, 25412–25422. https://doi.org/10.1021/ACSANM.4C04386.

(52) Li, M.-H.; Liu, S.-C.; Qiu, F.-Z.; Zhang, Z.-Y.; Xue, D.-J.; Hu, J.-S.; Li, M.-H.; Liu, S.-C.; Qiu, F.-Z.; Zhang, Z.-Y. D.; Xue, -J; Hu, J.-S. High-Efficiency CsPbI2Br Perovskite Solar Cells with Dopant-Free Poly(3-Hexylthiophene) Hole Transporting Layers. *Adv Energy Mater* **2020**, *10* (21), 2000501. https://doi.org/10.1002/AENM.202000501.

(53) Luo, T.; Liu, L.; Du, M.; Wang, K.; Liu, S. Vacuum Preparation of Charge Transport Layers for Perovskite Solar Cells and Modules. *J Mater Chem A Mater* **2025**, *13* (3), 1669–1710. https://doi.org/10.1039/D4TA06502F.

(54) Li, B.; Zhang, Y.; Fu, L.; Yu, T.; Zhou, S.; Zhang, L.; Yin, L. Surface Passivation Engineering Strategy to Fully-Inorganic Cubic CsPbI3 Perovskites for High-Performance Solar Cells. *Nature Communications 2018 9:1* **2018**, *9* (1), 1–8. https://doi.org/10.1038/s41467-018-03169-0.

(55) Qiu, W.; Paetzold, U. W.; Gehlhaar, R.; Smirnov, V.; Boyen, H. G.; Tait, J. G.; Conings, B.; Zhang, W.; Nielsen, C. B.; McCulloch, I.; Froyen, L.; Heremans, P.; Cheyns, D. An Electron Beam Evaporated TiO2 Layer for High Efficiency Planar Perovskite Solar Cells on Flexible Polyethylene Terephthalate Substrates. *J Mater Chem A Mater* **2015**, *3* (45), 22824–22829. https://doi.org/10.1039/C5TA07515G.

(56) Ke, W.; Fang, G.; Wang, J.; Qin, P.; Tao, H.; Lei, H.; Liu, Q.; Dai, X.; Zhao, X. Perovskite Solar Cell with an Efficient TiO2 Compact Film. *ACS Appl Mater Interfaces* **2014**, *6* (18), 15959–15965. https://doi.org/10.1021/am503728d.

(57) Kim, I. S.; Cao, D. H.; Buchholz, D. B.; Emery, J. D.; Farha, O. K.; Hupp, J. T.; Kanatzidis, M. G.; Martinson, A. B. F. Liquid Water- and Heat-Resistant Hybrid Perovskite Photovoltaics via an Inverted ALD Oxide Electron Extraction Layer Design. *Nano Lett* **2016**, *16* (12), 7786–7790. https://doi.org/10.1021/acs.nanolett.6b03989.

(58) Moseley, O. D. I.; Roose, B.; Zelewski, S. J.; Stranks, S. D. Identification and Mitigation of Transient Phenomena That Complicate the Characterization of Halide Perovskite Photodetectors. *ACS Appl Energy Mater* **2023**, *6* (20), 10233–10242. https://doi.org/10.1021/acsaem.2c03453.

(59) Jiang, F.; Shi, Y.; Rana, T. R.; Morales, D.; Gould, I. E.; McCarthy, D. P.; Smith, J. A.; Christoforo, M. G.; Yaman, M. Y.; Mandani, F.; Terlier, T.; Contreras, H.; Barlow, S.; Mohite, A. D.; Snaith, H. J.; Marder, S. R.; MacKenzie, J. D.; McGehee, M. D.; Ginger, D. S. Improved Reverse Bias Stability in p–i–n Perovskite Solar Cells with Optimized Hole Transport Materials and Less Reactive Electrodes. *Nature Energy 2024 9:10* **2024**, *9* (10), 1275–1284. https://doi.org/10.1038/S41560-024-01600-Z.

(60) Ren, X.; Wang, J.; Lin, Y.; Wang, Y.; Xie, H.; Huang, H.; Yang, B.; Yan, Y.; Gao, Y.; He, J.; Huang, J.; Yuan, Y. Mobile Iodides Capture for Highly Photolysis- and Reverse-Bias-Stable Perovskite Solar Cells. *Nature Materials 2024 23:6* **2024**, *23* (6), 810–817. https://doi.org/10.1038/s41563-024-01876-2.

(61) Gould, I. E.; Xiao, C.; Patel, J. B.; McGehee, M. D. In-Operando Characterization of P-I-N Perovskite Solar Cells under Reverse Bias. In *Conference Record of the IEEE Photovoltaic Specialists Conference*; Institute of Electrical and Electronics Engineers Inc., 2021; pp 1365–1367. https://doi.org/10.1109/PVSC43889.2021.9518723.

(62) Sundar, C. S.; Bharathi, A.; Hariharan, Y.; Janaki, J.; Sankara Sastry, V.; Radhakrishnan, T. S. Thermal Decomposition of C60. *Solid State Commun* **1992**, *84* (8), 823–826. https://doi.org/10.1016/0038-1098(92)90098-T.

(63) Bracesco, A. E. A.; van Himste, J.; Kessels, W. M. M.; Zardetto, V.; Creatore, M. In Situ IR Spectroscopy Studies of Atomic Layer-Deposited SnO2 on Fullerenes for Perovskite Photovoltaics. *ACS Appl Mater Interfaces* **2024**, *16* (43), 59468–59476. https://doi.org/10.1021/ACSAMI.4C09630.

(64) Chen, C.; Zhang, S.; Wu, S.; Zhang, W.; Zhu, H.; Xiong, Z.; Zhang, Y.; Chen, W. Effect of BCP Buffer Layer on Eliminating Charge Accumulation for High Performance of Inverted Perovskite Solar Cells. *RSC Adv* **2017**, *7* (57), 35819–35826. https://doi.org/10.1039/C7RA06365B.

(65) Ye, F.; Zhang, S.; Warby, J.; Wu, J.; Gutierrez-Partida, E.; Lang, F.; Shah, S.; Saglamkaya, E.; Sun, B.; Zu, F.; Shoaee, S.; Wang, H.; Stiller, B.; Neher, D.; Zhu, W. H.; Stolterfoht, M.; Wu, Y. Overcoming C60-Induced Interfacial Recombination in Inverted Perovskite Solar Cells by Electron-Transporting Carborane. *Nature Communications 2022 13:1* **2022**, *13* (1), 1–12. https://doi.org/10.1038/s41467-022-34203-x.

(66) Al-Ashouri, A.; Köhnen, E.; Li, B.; Magomedov, A.; Hempel, H.; Caprioglio, P.; Márquez, J. A.; Vilches, A. B. M.; Kasparavicius, E.; Smith, J. A.; Phung, N.; Menzel, D.; Grischek, M.; Kegelmann, L.; Skroblin, D.; Gollwitzer, C.; Malinauskas, T.; Jošt, M.; Matič, G.; Rech, B.; Schlatmann, R.; Topič, M.; Korte, L.; Abate, A.; Stannowski, B.; Neher, D.; Stolterfoht, M.; Unold, T.; Getautis, V.; Albrecht, S. Monolithic Perovskite/Silicon Tandem Solar Cell with >29% Efficiency by Enhanced Hole Extraction. *Science (1979)* **2020**, *370* (6522), 1300–1309. https://doi.org/10.1126/science.abd4016.

(67) Zheng, X.; Jiang, T.; Bai, L.; Chen, X.; Chen, Z.; Xu, X.; Song, D.; Xu, X.; Li, B.; Yang, Y. Enhanced Thermal Stability of Inverted Perovskite Solar Cells by Interface Modification and Additive Strategy. *RSC Adv* **2020**, *10* (31), 18400–18406. https://doi.org/10.1039/D0RA03238G.

(68) Zhu, W.; Chai, W.; Chen, D.; Ma, J.; Chen, D.; Xi, H.; Zhang, J.; Zhang, C.; Hao, Y. High-Efficiency (>14%) and Air-Stable Carbon-Based, All-Inorganic CsPbI2Br Perovskite Solar Cells through a Top-Seeded Growth Strategy. *ACS Energy Lett* **2021**, *6* (4), 1500–1510. https://doi.org/10.1021/acsenergylett.1c00325.

(69) Song, W.; Zhang, X.; Lammar, S.; Qiu, W.; Kuang, Y.; Ruttens, B.; D'Haen, J.; Vaesen, I.; Conard, T.; Abdulraheem, Y.; Aernouts, T.; Zhan, Y.; Poortmans, J. Critical Role of Perovskite Film Stoichiometry in Determining Solar Cell Operational Stability: A Study on the Effects of Volatile A-Cation Additives. *ACS Appl Mater Interfaces* **2022**, *14* (24), 27922–27931. https://doi.org/10.1021/acsami.2c05241.

(70) Fu, F.; Pisoni, S.; Jeangros, Q.; Sastre-Pellicer, J.; Kawecki, M.; Paracchino, A.; Moser, T.; Werner, J.; Andres, C.; Duchêne, L.; Fiala, P.; Rawlence, M.; Nicolay, S.; Ballif, C.; Tiwari, A. N.; Buecheler, S. I2 Vapor-Induced Degradation of Formamidinium Lead Iodide Based Perovskite Solar Cells under Heat–Light Soaking Conditions. *Energy Environ Sci* **2019**, *12* (10), 3074–3088. https://doi.org/10.1039/C9EE02043H.

(71) Khadka, D. B.; Shirai, Y.; Yanagida, M.; Miyano, K. Insights into Accelerated Degradation of Perovskite Solar Cells under Continuous Illumination Driven by Thermal Stress and Interfacial Junction. *ACS Appl Energy Mater* **2021**, *4* (10), 11121–11132. https://doi.org/10.1021/acsaem.1c02037.
(72) Younes, E. M.; Gurung, A.; Bahrami, B.; El-Maghraby, E. M.; Qiao, Q. Enhancing Efficiency and Stability of Inverted Structure Perovskite Solar Cells with Fullerene C60 Doped PC61BM Electron Transport Layer. *Carbon N Y* **2021**, *180*, 226–236. https://doi.org/10.1016/J.CARBON.2021.05.008.
(73) Huang, Y.; Yin, W. J.; He, Y. Intrinsic Point Defects in Inorganic Cesium Lead Iodide Perovskite CsPbI3. *Journal of Physical Chemistry C* **2018**, *122* (2), 1345–1350. https://doi.org/10.1021/acs.jpcc.7b10045.
(74) Kang, J.; Wang, L. W. High Defect Tolerance in Lead Halide Perovskite CsPbBr3. *Journal of Physical Chemistry Letters* **2017**, *8* (2), 489–493. https://doi.org/10.1021/acs.jpclett.6b02800.
(75) Chu, W.; Saidi, W. A.; Zhao, J.; Prezhdo, O. V. Soft Lattice and Defect Covalency Rationalize Tolerance of β-CsPbI3 Perovskite Solar Cells to Native Defects. *Angewandte Chemie International Edition* **2020**, *59* (16), 6435–6441. https://doi.org/10.1002/ANIE.201915702.
(76) Neophytou, M.; De Bastiani, M.; Gasparini, N.; Aydin, E.; Ugur, E.; Seitkhan, A.; Moruzzi, F.; Choaie, Y.; Ramadan, A. J.; Troughton, J. R.; Hallani, R.; Savva, A.; Tsetseris, L.; Inal, S.; Baran, D.; Laquai, F.; Anthopoulos, T. D.; Snaith, H. J.; De Wolf, S.; McCulloch, I. Enhancing the Charge Extraction and Stability of Perovskite Solar Cells Using Strontium Titanate (SrTiO3) Electron Transport Layer. *ACS Appl Energy Mater* **2019**, *2* (11), 8090–8097. https://doi.org/10.1021/acsaem.9b01567.
(77) Hwang, I.; Mcneill, C. R.; Greenham, N. C. Drift-Diffusion Modeling of Photocurrent Transients in Bulk Heterojunction Solar Cells. *J Appl Phys* **2009**, *106*, 94506. https://doi.org/10.1063/1.3247547.
(78) Mcneill, C. R.; Hwang, I.; Greenham, N. C. Photocurrent Transients in All-Polymer Solar Cells: Trapping and Detrapping Effects. *J Appl Phys* **2009**, *106*, 24507. https://doi.org/10.1063/1.3177337.
(79) Burkhard, G. F.; Hoke, E. T.; McGehee, M. D. Accounting for Interference, Scattering, and Electrode Absorption to Make Accurate Internal Quantum Efficiency Measurements in Organic and Other Thin Solar Cells. *Advanced Materials* **2010**, *22* (30), 3293–3297. https://doi.org/10.1002/ADMA.201000883.
(80) Fischer, M.; Tvingstedt, K.; Baumann, A.; Dyakonov, V. Doping Profile in Planar Hybrid Perovskite Solar Cells Identifying Mobile Ions. *ACS Appl Energy Mater* **2018**, *1* (10), 5129–5134. https://doi.org/10.1021/acsaem.8b01119.
(81) Goushcha, A. O.; Tabbert, B. On Response Time of Semiconductor Photodiodes. *Optical Engineering* **2017**, *56* (09), 097101. https://doi.org/10.1117/1.oe.56.9.097101.
(82) Pham, H. M.; Naqvi, S. D. H.; Tran, H.; Tran, H. Van; Delda, J.; Hong, S.; Jeong, I.; Gwak, J.; Ahn, S. J. Effects of the Electrical Properties of SnO2 and C60 on the Carrier Transport Characteristics of P-i-n-Structured Semitransparent Perovskite Solar Cells. *Nanomaterials* **2023**, *13* (13), 3091. https://doi.org/10.3390/nano13243091.
(83) Klipfel, N.; Alvarez, A. O.; Kanda, H.; Adrian Sutanto, A.; Igci, C.; Roldán-Carmona, C.; Momblona, C.; Fabregat-Santiago, F.; Khaja Nazeeruddin, M. C60 Thin Films in Perovskite Solar Cells: Efficient or Limiting Charge Transport

Layer? *ACS Appl. Energy Mater* **2022**, *2022*, 1646–1655. https://doi.org/10.1021/acsaem.1c03060.

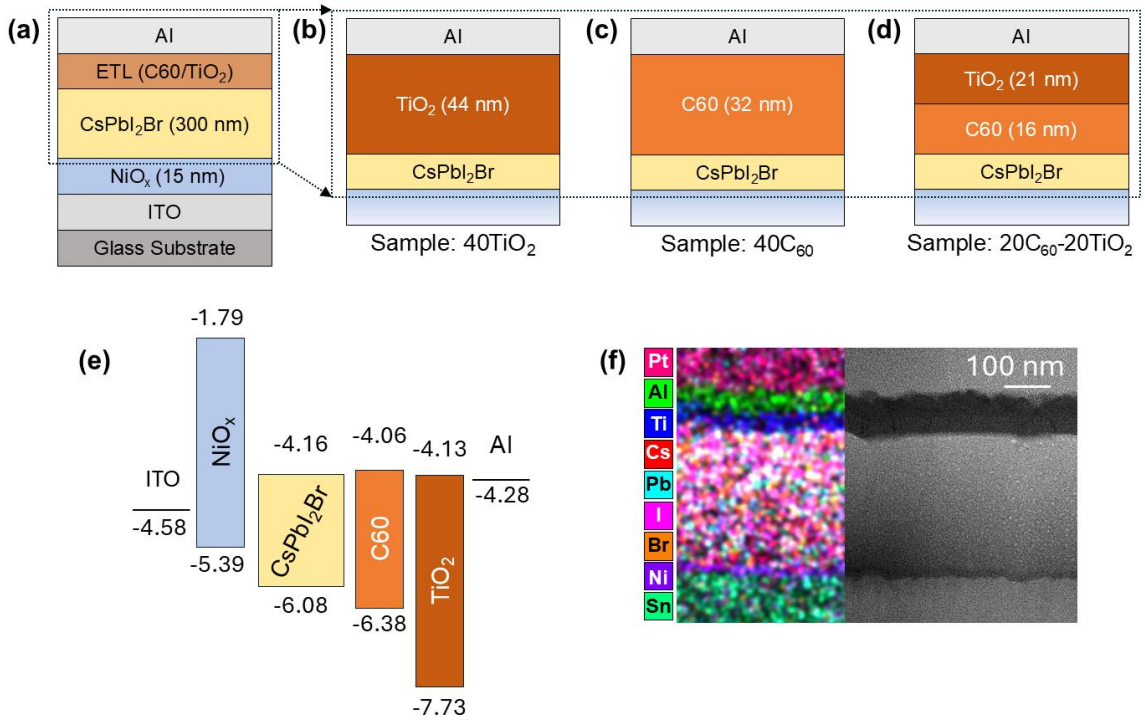

Figure 1: (a) Schematic of the diode structure for vacuum deposited all-inorganic perovskite photodetectors. Variations of the ETL used in this study, including (b) a single 40 nm TiO_2 layer, (c) a single 40 nm C_{60} layer, and (d) a C_{60} – TiO_2 bilayer, each 20 nm thick. The samples are named according to the nominal thickness of their ETL, while the value in the parenthesis indicates the real thickness measured through their scanning transmission electron microscopy (STEM) cross-section (**Fig. S2**). (e) Energy levels of the stack's constituent layers. (f) STEM high-angle annular dark field (HAADF) image of the $40TiO_2$ sample, superimposed with the energy dispersive X-Ray spectroscopy (EDS) elemental mapping.

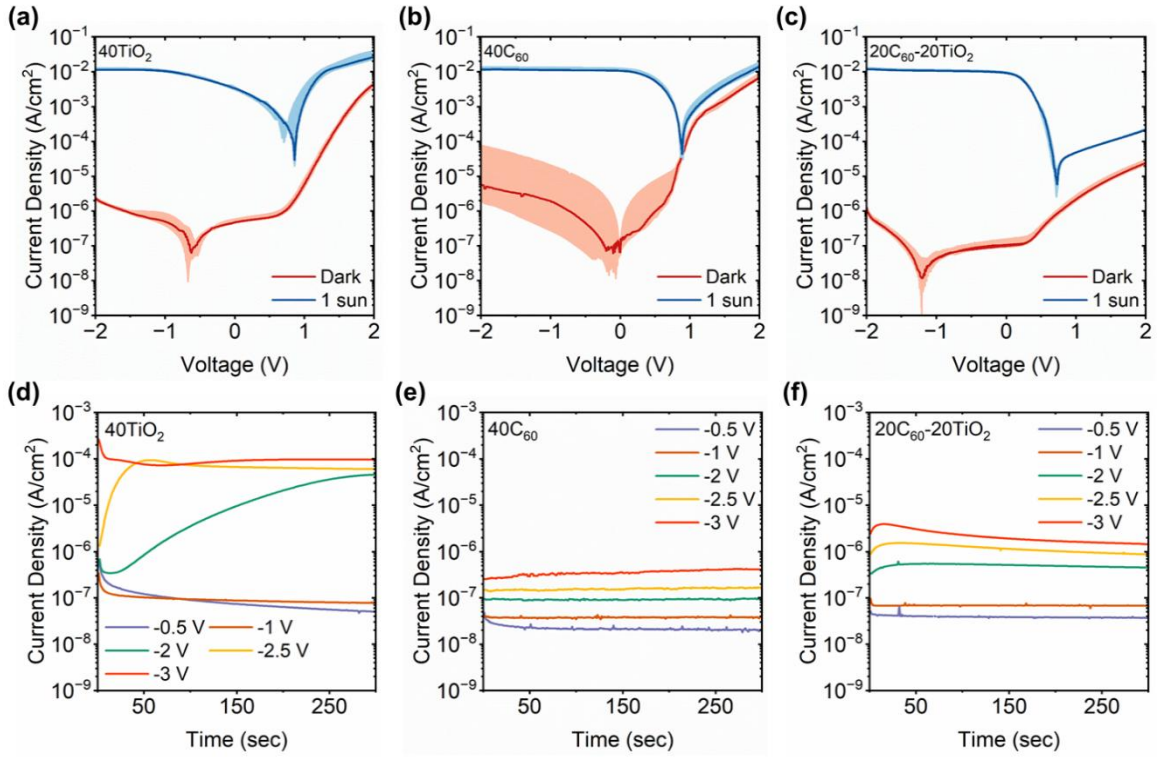

Figure 2: Statistical representation of the PePD's current density as a function of bias in darkness and under simulated 1 sun illumination (100 mW/cm^3 - AM 1.5G) for the stacks with (a) 40 nm of TiO_2, (b) 40 nm of C_{60}, and (c) 20 nm of C_{60} and 20 nm of TiO_2 as the ETL. For each curve, the solid line represents the median response among 12 devices that were fabricated on the same substrate, while the shaded area represents the interquartile range. Dark current density as a function of time under increasing steps of reverse bias for stacks with (d) 40 nm of TiO_2, (e) 40 nm of C_{60}, and (f) 20 nm of C_{60} and 20 nm of TiO_2 as the ETL. Each bias step was maintained for 300 s and between two consecutive steps the device was allowed to recover for an additional 300 s in darkness.

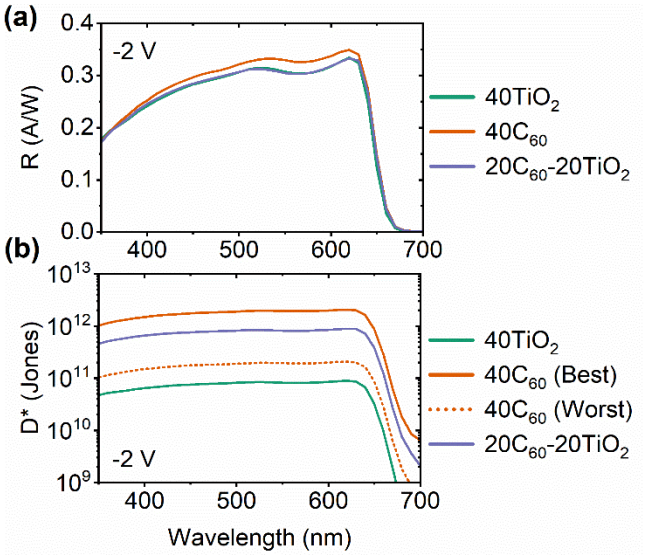

Figure 3: (a) Responsivity and (b) specific detectivity of PePDs with ETLs with different C_{60} to TiO_2 thickness ratio as a function of wavelength. For the C_{60} sample, we considered the specific detectivity of both the best-performing device, characterized by the lowest J_d, and the worst-performing device, assuming a J_d two orders of magnitude higher.

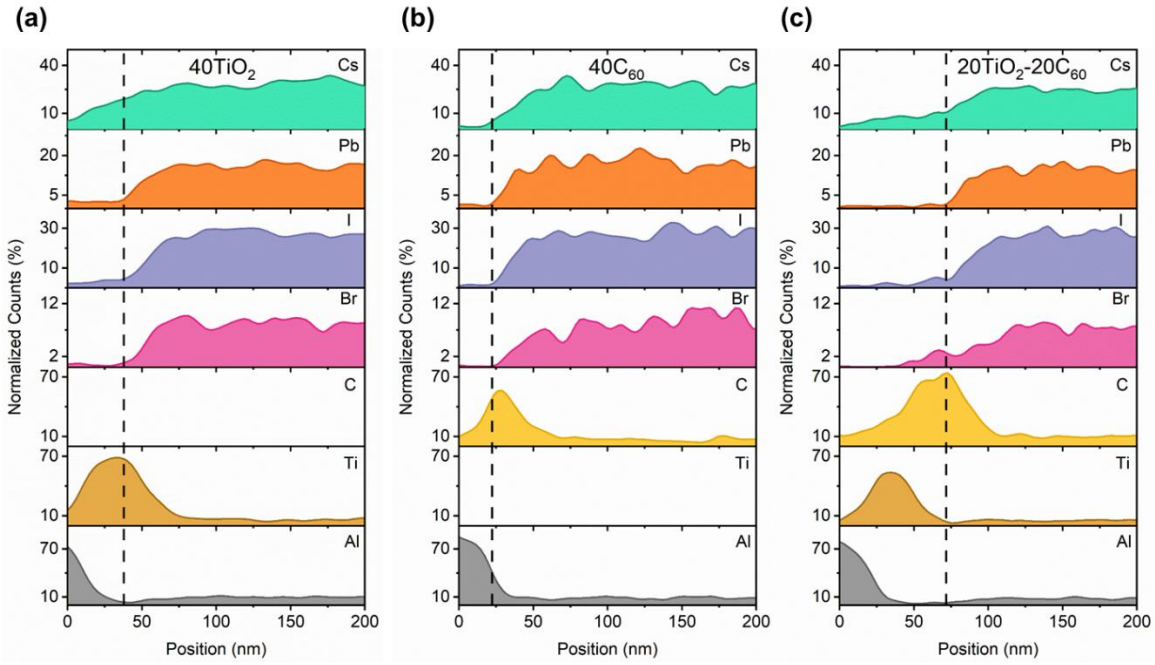

Figure 4: EDS elemental concentration profiles for the PePD with a) 40 nm of TiO_2, (b) 40 nm of C_{60}, and (c) 20 nm of C_{60} and 20 nm of TiO_2 as the ETL. The counts have been normalized with respect to the total amount of counts at each position. The dashed line indicates the start of the perovskite layer, having as reference the onset of the Pb signal.

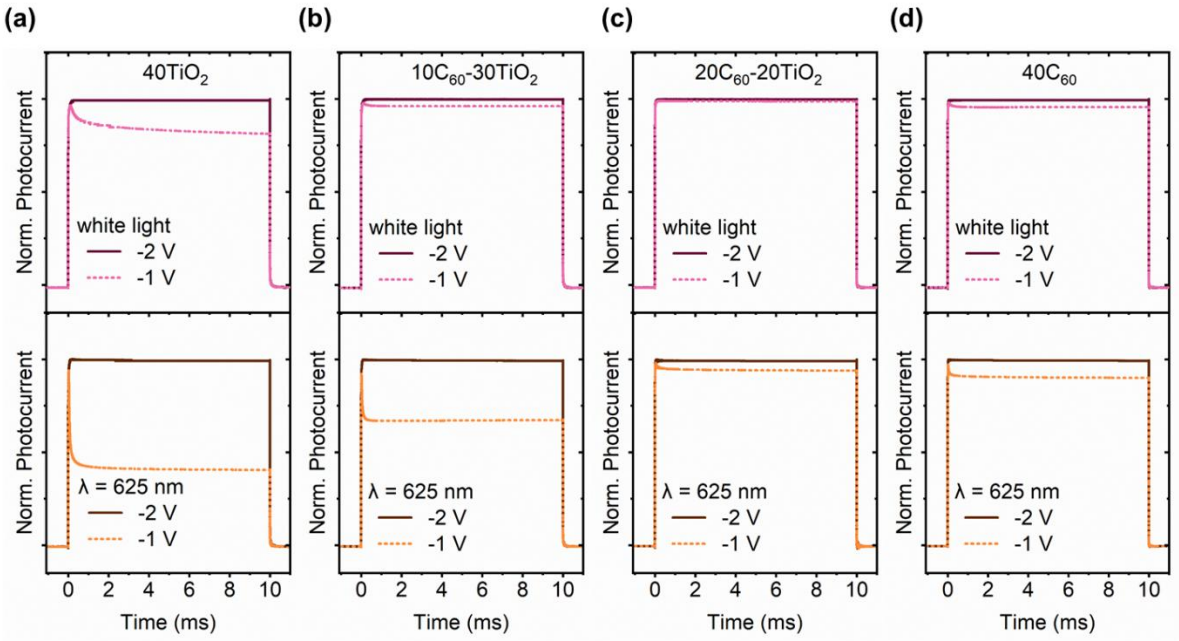

Figure 5: TPC response of PePDs with (a) 40 nm of TiO_2, (b) 10 nm of C_{60} and 30 nm of TiO_2, (c) 20 nm of C_{60} and 20 nm of TiO_2, and (d) 40 nm of C_{60} as the ETL. For each stack and illumination profile, the photocurrent transients have been normalized with respect to the photocurrent response at -2 V.

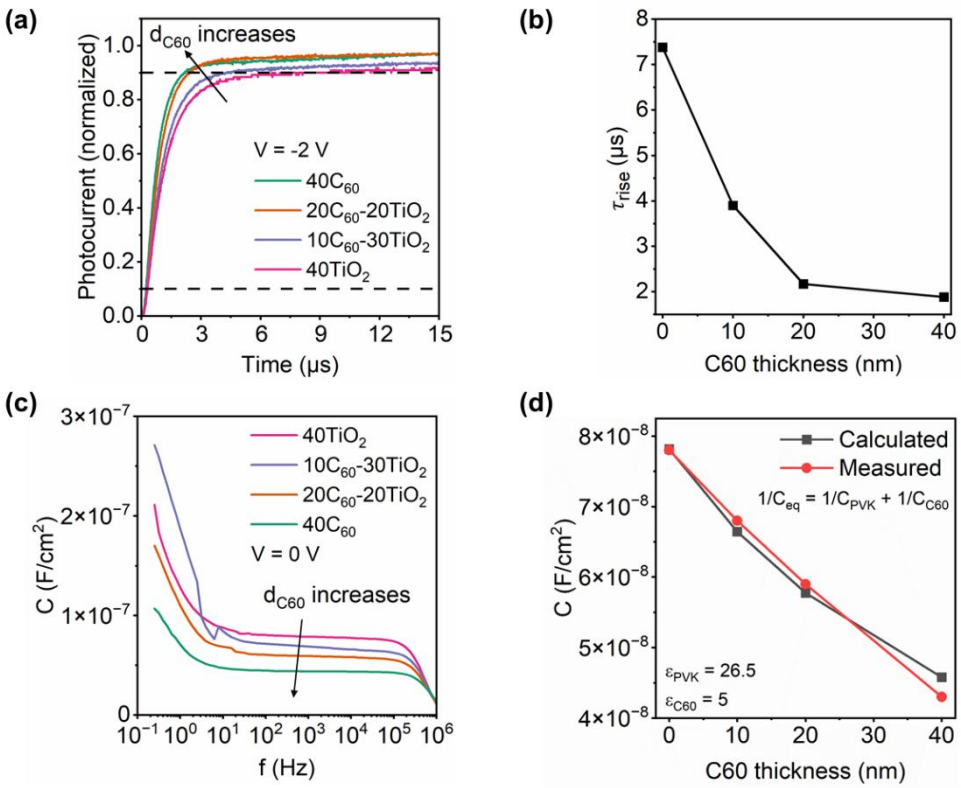

Figure 6: (a) Comparison of TPC response speed of PePDs with ETLs with different C_{60} to TiO_2 thickness ratio under white light illumination, biased at -2 V. (b) Dependence of the PePD's rise time on the thickness of the C_{60} layer deposited on top of the perovskite layer. (c) Comparison of capacitance as a function of frequency for PePDs with ETLs with different C_{60} to TiO_2 thickness ratio. (d) Comparison of the experimentally measured device capacitance (10^3 Hz) with the analytically calculated one as a function of the thickness of the C_{60} layer deposited on top of the perovskite layer. For the analytical calculation, it was assumed that both the perovskite and the C_{60} layer are fully depleted.

C [F/cm^2]	7.8×10^{-8}
ε_0[F/m]	8.85×10^{-12}
d $CsPbI_2Br$ [nm]	300
A [cm^2]	0.125

Table 1: Parameters used for the estimation of the perovskite's ε_r according to the capacitance measurements of the $40TiO_2$ sample.

C_{eq} [F/cm^2]	2.4×10^{-8}
ε_0 [F/m]	8.85×10^{-12}
ε_r SiO_2	3.9
d SiO_2 [nm]	100
d $CsPbI_2Br$ [nm]	300
A [cm^2]	0.16

Table 2: Parameters used for the estimation of the perovskite's ε_r according to the capacitance measurements of the MOS structure.

Table of Contents Figure